

1 **Spatiotemporal Heterogeneity of b Values Revealed by a
2 Data-Driven Approach for June 17, 2019 M_S 6.0,
3 Changning Sichuan, China Earthquake Sequence**

4 Changsheng Jiang^{1*}, Libo Han¹, Feng Long², Guijuan Lai¹, Fengling Yin¹, Jinmeng Bi³,
5 Zhengya Si⁴

6 ¹ Institute of Geophysics, China Earthquake Administration, Beijing 100081, China

7 ² Sichuan Earthquake Agency, Chengdu 610041, China

8 ³ Tianjin Earthquake Agency, Tianjin 300201, China

9 ⁴ Beijing Earthquake Agency, Beijing 100080, China

10 *Correspondence to:* Changsheng Jiang (jiangcs@cea-igp.ac.cn)

11 **Abstract.** The spatiotemporal heterogeneity of b values has great potential for understanding the
12 seismogenic process and assessing the seismic hazard. However, there is still much controversy about
13 whether it exists or not, and an important reason is that the choice of subjective parameters has eroded
14 the foundations of many researches. To overcome this problem, we used a recent developed non-
15 parametric method based on the data-driven concept to calculate b values. The major steps of this method
16 include: 1) perform a large number of Voronoi tessellation, Bayesian information criterion (BIC) value
17 calculation and selection of the optimal models for the study area, and 2) use the ensemble median (Q_2)
18 and median absolute deviation (MAD) value to represent the final b value and its uncertainty. We
19 investigated spatiotemporal variations of b values before and after the 2019 Changning M_S 6.0 earthquake
20 in Sichuan Basin, China. The results reveal a spatial volume with low pre-mainshock b values near the
21 mainshock source region, and its size corresponds roughly with the rupture area of the mainshock. The
22 anomalously high pre-mainshock b values distributed in the NW direction of the epicenter was
23 interpreted to be related with fluid invasion. The decreases of b values during the aftershock sequence
24 along with the occurrences of several strong aftershocks imply that b values could be an indicator of
25 stress state. In addition, we found that although the distribution characteristics of b values obtained from
26 different way of investigating are qualitatively consistent, they differ significantly in terms of their
27 specific values, suggesting that the best way to study the heterogeneous pattern of b values is in the joint
28 dimension of space-time rather than alone in time and space. Overall, our study emphasizes the
29 importance of b value studies on assessing the earthquake hazards.

30 **Keywords** b value; data-driven; spatiotemporal heterogeneity; Ogata-Katsura 1993 model; Voronoi
31 tessellation

32 **Introduction**

33 The Gutenberg-Richter b value describes the corresponding frequency-magnitude distribution (FMD)
34 characteristics by reflecting the relative proportion of the frequency of large and small earthquakes within
35 a given space-time range. It is considered to be related to the stress conditions in the Earth's crust (e.g.,
36 Wyss, 1973; Urbancic et al., 1992; Mori and Abercrombie, 1997; Toda et al., 1998), complexity of the
37 fault trace (Stirling et al., 1996), and the extent of creep (Amelung and King, 1997) and other factors.
38 Experimental studies in the laboratory have shown that a weak and less resistant environment under
39 stress would produce a high b value, while materials that are more compact and more resistant under
40 pressure do not fail, which leads to a reasonable low b value (Aktar et al., 2004). In the case where the
41 material and structure are clarified, decreasing b value is considered to be related to increasing stress
42 (Scholz, 1968) or pore pressure diffusion (Hainzl and Fischer, 2002; Lei and Satoh, 2007). For the above
43 reasons, b value has been widely concerned in seismogenic environment analysis and seismic hazard
44 research.

45 Spatial and temporal heterogeneity is an important topic in b value research, especially under the
46 assumption that the local b values are inversely dependent on the applied shear stress, and that low b
47 values ($b < 0.7$) can reflect the existence of locked faults or asperities. Therefore, the spatial and temporal
48 heterogeneity of b values is considered as an important clue for forecasting the location and size of
49 potential large earthquakes (Wiemer and Wyss, 1997; Schorlemmer and Wiemer, 2005; Murru et al.,
50 2007). Using the spatial heterogeneity of b value to identify possible asperities is performed in some
51 cases, such as the San Jacinto-Elsinore fault system in southern California (Wyss et al., 2000), the
52 Parkfield segment of the San Andreas fault (Wiemer and Wyss, 1997), and the case study of the 2014
53 Parkfield $M 6.0$ earthquake (Schorlemmer and Wiemer, 2005).

54 A model named Asperity Likelihood Model (ALM) based on the above assumptions has been developed
55 and used to forecast future earthquakes (Wiemer and Schorlemmer, 2007; Gulia et al., 2010). The
56 research on the temporal heterogeneity of b values mainly includes using b value time variation of early
57 aftershock sequence and the constructed system of foreshock traffic light system (FTLS) to evaluate the
58 risk of subsequent larger aftershocks (Gulia and Wiemer, 2019).

59 However, some research results show that the apparent variability of b values is not significant in some
60 cases (Del Pezzo et al., 2003). For example, Amorèse et al. (2010) systematically examined the variation

61 of b values in Southern California to the depth of the crust, and found that the hypothesis was not
62 statistically significant. By using a data-driven approach, Kamer and Hiemer (2015) shows that the
63 spatial b values in most locations in California are distributed within a very limited range (0.94 ± 0.04 –
64 1.15 ± 0.06), and the previously reported spatial b value variation is overestimated and mainly due to the
65 subjective choice of parameters. Besides, the spatial and temporal heterogeneity of b values is also
66 considered to be due to the subjective arbitrariness of the calculation rules and the lack of statistical
67 robustness (Kagan 1999).

68 Based on the above viewpoints, the calculation reliability for researches on the spatiotemporal
69 heterogeneity of b values still needs to be solved, and the relationship between the spatiotemporal
70 variation process of b values and the occurrence of strong earthquakes need to be investigated for more
71 earthquake cases. In this study, we will utilize data-driven based b values calculation methods that have
72 been developed in recent years (Kamer and Hiemer, 2015; Nandan et al., 2017; Si and Jiang, 2019) for
73 case studies of the 2019 Changning M_S 6.0 earthquake in Sichuan, China.

74 **Method**

75 In the traditional calculation of the Gutenberg-Richter magnitude-frequency b value, a fixed number of
76 earthquakes (Hutton et al., 2010; Ogata, 2011) or a fixed minimum and maximum selection radius
77 (Woessner and Wiemer, 2005) are generally used to select data and the maximum likelihood estimation
78 is used to obtain b values. Because such calculations have strong subjectivity in calculating rules, it has
79 caused widespread controversy. The data-driven approaches to seismicity parameter calculation have
80 been gradually developed in recent years (Sambridge et al., 2013; Kamer and Hiemer, 2015; Nandan et
81 al., 2017; Si and Jiang, 2019), by using the Voronoi tessellation to create a large number of spatially
82 random grids and covering the possibility of segmentation of spatial regions, relying on the Bayesian
83 information criterion (BIC) to select a part of the optimal models with the smallest BIC value, and
84 representing the final result of seismic activity parameters through the ensemble median value. Because
85 the data-driven approach uses an automatic parametric calculation, it provides a possibility for solving
86 the subjective problem of earthquake data selection.

87 Among those data-driven approaches, Si and Jiang (2019) developed a method using continuous
88 distribution function (hereafter referred to as OK1993 model) given by Ogata and Katsura (1993), which

89 has the advantage of simultaneously determining the minimum magnitude of completeness and obtaining
90 b values. In this paper, we will use this approach to study the spatiotemporal heterogeneity of b values
91 for the 2019 Changning M_S 6.0 earthquake.

92 The OK1993 model uses the seismic detection rate function $q(M)$ to describe the complete detection
93 degree of earthquake events with different magnitudes in the magnitude-frequency distribution:

$$94 \quad q(M|\mu, \sigma) = \frac{1}{\sqrt{2\pi\sigma^2}} \int_{-\infty}^M e^{-\frac{(x-\mu)^2}{2\sigma^2}} dx \quad (1)$$

95 where M is the magnitude, the parameter μ represents the corresponding magnitude to the detection rate
96 of 50%, and σ indicates the corresponding magnitude range. The actual earthquake probability density
97 function and the log-likelihood function of the OK1993 model can be expressed as:

$$98 \quad P(M|\beta, \mu, \sigma) = \frac{e^{-\beta M} q(M|\mu, \sigma)}{\int_{-\infty}^{+\infty} e^{-\beta M} q(M|\mu, \sigma) dM} = \beta e^{-\beta(M-\mu)+\beta^2\sigma^2/2} q(M|\mu, \sigma) \quad (2)$$

$$99 \quad \ln L(\theta) = n \ln \beta - \sum_{i=1}^n [\beta M_i - \ln q(M_i|\mu, \sigma)] + n\beta\mu - \frac{n}{2}\beta^2\sigma^2 \quad (3)$$

100 The $\{M_1, M_2, \dots, M_n\}$ in the above formula is the magnitude of a given series of observational events and
101 the power exponent $\beta = b \ln 10$, The parameter $[\beta, \mu, \sigma]$ can be obtained by fitting the above formula
102 using the maximum likelihood method. The Bayesian information criterion $BIC = -\ln L(\theta) +$
103 $k/2 \ln (n)$ be adopted to calculate the corresponding BIC value and select the optimal models. Since
104 each grid node is composed of spatial coordinates $[x, y]$ and three parameters $[\beta, \mu, \sigma]$ in the OK1993
105 model, so the total number of freedom degrees is $k = 5 \times \text{num of node}$ in the entire study region.

106 The construction of the data-driven approach can be achieved by the Voronoi tessellation with limited
107 boundaries. Voronoi tessellation refer to a unique set of continuous polygon partitioning schemes $\{P_i, i$
108 $= 1, 2, \dots, n\}$ given by a set of spatial nodes $S = \{s_1, s_2, \dots, s_n\}$ in two-dimensional or three-dimensional
109 space. The polygon $P_i = \{x \mid \text{dist}(x, s_i) \leq \text{dist}(x, s_j), i \neq j\}$, where $\text{dist}(a, b)$ denotes the Euclidean distance
110 between two points. Voronoi tessellation also benefits from the uniqueness of its spatial division, so it is
111 widely used in computing science, political elections, and many other studies (Rubner et al., 2000; Svec
112 et al., 2007). The calculation steps of the data-driven approach include: (1) randomly throwing a certain
113 number of nodes in the study area and performing Voronoi meshing, with the number of grid nodes
114 gradually increasing from 2 to 40. To ensure that the Voronoi tessellation covers the possibility of various
115 spatial region segmentation, each number of grid nodes is randomly thrown 100 times. (2) Calculate
116 OK1993 model parameters and BIC values for $(2 + 3 + \dots + 40) \times 100 = 81900$ Voronoi cells obtained from
117 3900 tessellations (or spatial calculation models). Sum the BIC values of all the Voronoi cells obtained

118 from each tessellation and use it as the basis for judging whether this spatial calculation model is the
119 optimal model; (3) Among the 3900 spatial calculation models, 100 models (marked as best-100) with
120 smaller BIC values were selected as the optimal models, and the parameters $[\beta, \mu, \sigma]$ of the ensemble
121 median (Q_2) and median absolute deviation (MAD) were used as the final calculation results. The b value
122 can be obtained by $b = \beta/\ln 10$.

123 The maximum likelihood calculation of the OK1993 model parameter is not performed for the number
124 of earthquakes $N_1 < 5$ contained in a Voronoi cell, so the actual number of effective cells N_v obtained by
125 each tessellation is used, to distinguish the number of randomly thrown nodes. Although the value of N_1
126 may affect the parameter fitting error in some polygons with a small number of events, considering that
127 the OK1993 model in the form of continuous distribution function has the advantage of obvious fit
128 adaptability compared to the traditional linear Frequency-Magnitude Distribution (FMD) function in a
129 small number of data cases, this setting also ensures that the spatial division can obtain more polygon
130 calculation results, and the final result of the parameters is expressed by the ensemble median value, so
131 the effect of this method of value-taking on the final result is minimal.

132 In the above calculation steps, the setting of the maximum number of nodes, the number of random
133 throws, etc. has obvious subjectivity. However, due to the fact that the data-driven approach actually
134 obtains a very stable final result when the number of divisions and the number of grid nodes are sufficient
135 (Si and Jiang, 2019), for example, when the maximum number of nodes is 100, each type of nodes are
136 randomly thrown 1000 times, and the final result obtained when 1000 optimal models are selected is
137 almost the same as the result of this paper.

138 **Study Region and Data Used**

139 The 2019 Changning M_S 6.0 earthquake sequence occurred in the basin-mountain junction in the southern
140 margin of the Sichuan Basin, where the tectonic activity is relatively weak. The seismicity in the area is
141 mainly controlled by folds and associated faults. The intensity of historically destructive earthquakes is
142 low in the area where aftershocks extend. No earthquake with magnitude above 5.0 has been recorded in
143 this area before the Changning M_S 6.0 earthquake. According to Yi et al. (2019), it is inferred that the
144 occurrence of the Changning M_S 6.0 earthquake sequence may be related to the Baixiangyan-Shizitan
145 anticline and the Shuanghechang anticline and their associated fault activities. Figure 1 shows the study
146 area of this paper. We will focus on the rectangular area A'B'C'D' where the aftershock sequence mainly

147 occurred and the rectangular area ABCD where the surrounding earthquakes are active.

148 We used earthquake catalogs and bulletins provided by the Sichuan Regional Seismic Network from

149 2009/01/01 to 2019/07/17. To obtain relatively reliable parameters such as the epicenter location and

150 focal depth, the double-difference algorithm HypoDD (Waldhauser and Ellsworth, 2000) was used to

151 relocate the earthquakes. Among the data we used, a total of 21246 seismic events that meet the

152 requirements of the HypoDD method are not less than 4 arrivals, including 516649 P-wave arrivals,

153 506809 S-wave arrivals, and 59 permanent seismic stations and temporary seismic stations are used

154 which are located in Sichuan and surrounding provinces. We used a 12-layer one-dimensional crustal

155 velocity model (Xie et al., 2012) during the relocation. The ratio of V_p to V_s is set to 1.730.

156 A total of 18371 earthquake events were relocated (Fig. 1), of which the smallest event had a magnitude

157 of -1.0. Among them, 13728 and 4642 earthquakes before and after the M_s 6.0 mainshock, respectively.

158 The horizontal and vertical uncertainties are 0.425 km, 0.457 km and 0.654 km, respectively. The average

159 root mean square (RMS) of the travel-time residuals [of the locations](#) was reduced to 0.162 s. [In addition,](#)

160 [a total of 2875 events were discarded, accounting for 13.53% of the number of earthquakes in the original](#)

161 [catalog, and most](#) of their magnitudes range between M_L 0.3 to M_L 1.4 (corresponding to the intervals of

162 cumulative number 10% ~ 90%). Considering that the data-driven approach used in this paper is the

163 selection and ensemble averaging of a large number of random space partitioning schemes, and that the

164 OK1993 model is a continuous function of the magnitude-frequency distribution, the effect of these

165 excluded events on the calculation result of b value can be ignored.

166 From the spatial distribution of the relocated earthquakes shown in Figure 1, the aftershocks are mainly

167 distributed in the northwest direction of the mainshock epicenter and extend along the Changning

168 anticline with a length about 27 km, which is much longer than the rupture scale of about 10 km for a M

169 6 earthquake accordance with the empirical formula given by Well and Coppersmith (1994). Besides,

170 the shape of the aftershock distribution is not simply linear; there are obvious inflections in the middle

171 segment, and in the northwest there is a branch approximately perpendicular to the direction of aftershock

172 distribution. There are relatively few aftershocks near the epicenter of the mainshock, and a large number

173 of aftershocks occurred in the northwest.

174 In the aftershock sequence of the Changning M_s 6.0 earthquake, there are 4 aftershocks with magnitudes

175 exceeding M_s 5.0, which are 2019/06/17 M_s 5.1, 2019/06/18 M_s 5.3, 2019/06/22 M_s 5.4, and 2019/07/04

176 M_s 5.6 earthquake, respectively.

删除了: There were 2875 events were discarded, which accounted for 13.53% of original catalogue. Most

179



180

Fig. 1

181 To facilitate the calculation of b values and the display of the results, we have selected only the events
182 within the rectangular area A'B'C'D' where almost all aftershocks are concentrated and the rectangular
183 area ABCD where a large number of earthquakes existed before the mainshock occurred. The positions
184 of these earthquakes were transformed by Cartesian coordinates and rotated according to the origin point
185 (104.986°E, 28.395°N) of the coordinates so that the aftershock sequence can be spread horizontally in
186 the new coordinate system. The epicenter distribution after coordinate transformation in Figure 2a-c
187 shows the spatiotemporal distribution on the distance versus rank of index 2-D map of the earthquake
188 within the rectangular frame A'B'C'D'.

189



190

Fig. 2

191 **Spatial Distributions of b Values on Surface and Depth Profiles**

192 According to the technical process of the data-driven approach described above, after Voronoi
193 tessellation, calculation of the BIC values, and selection of the optimal models, the ensemble median (Q_2)
194 and ensemble median absolute deviation (MAD) of b values can be obtained. Figure 3 shows an example
195 of calculating the parameters of the OK1993 model in terms of the frequency-magnitude distribution
196 based on a data-driven approach. Figure 3a is the distribution of those BIC values corresponding to the
197 number of effective cells N_v , and the red dots are the selected best-100 models. Figure 3b shows an
198 example in the best-100 models, that is, in the case of $N_v = 20$, the Voronoi tessellation in the rectangular
199 study area ABCD and the distribution of b values obtained by its calculation. Figure 3c shows an example
200 of the fitting result of the Ogata-Katsura 1993 model corresponding to a cell in Figure 3b. The OK1993
201 model parameters obtained by the fitting are $b = 0.714$, $\mu = 0.376$ and $\sigma = 0.247$.

202



203

Fig. 3

204 We calculated the distribution of the ensemble median b value in the rectangular region ABCD and the
205 depth profile of the rectangular region A'B'C'D', respectively. The results are shown in Figure 4. Figures

206 4a-b are the results before the Changning M_s 6.0 earthquake and the entire study period, respectively. The
207 results show that the b values exhibit a strong heterogeneous spatial distribution in the rectangular region
208 ABCD before the Changning M_s 6.0 earthquake. Low b values are mainly distributed in the eastern half
209 of the area, with its lowest value being $b = 0.732$ and located near the epicenter of the mainshock. Low
210 b value contours are mainly distributed in the NE-SW direction and are consistent with the direction of
211 Shuanghechang anticline and their associated faults passing through the main epicenter. In the western
212 part of the rectangular region ABCD, high b values are distributed, with a largest value of $b = 2.200$.
213 This indicates that before the Changning M_s 6.0 earthquake, the differential stress near the epicenter of
214 the mainshock was high, but the spatial scale of this larger differential stress was much smaller than the
215 scale of the aftershock spatial distribution. The spatial distribution of b values calculated using all seismic
216 events (see Fig. 4b) shows that the area with low b values in the region ABCD is significantly enlarged,
217 and the b values in the rectangular region A'B'C'D' are almost less than 1.0 and further reduced to 0.698
218 near the epicenter of the mainshock. This phenomenon of a significant decrease in b value of the
219 aftershock sequence after the mainshock widely exists in many earthquake cases (El-Isaa and Eatonb,
220 2014; Gulia and Wiemer, 2019).
221 Figures 4c-d show the distribution of ensemble median b value on the depth profile of the rectangular
222 area A'B'C'D', and correspond to the results before the Changning M_s 6.0 earthquake and all study periods,
223 respectively. The calculation results after considering the depth information of the earthquake show that
224 b values also have strong heterogeneity at different depths. Among them, in Figure 4c, low b values are
225 mainly distributed at depth of 4 ~ 15 km and contains the source of the Changning M_s 6.0 earthquake
226 and the 2019/06/17 M_s 5.1 earthquake. The lowest b value is about 0.493, which is much smaller than
227 the minimum value in Figure 4a. In Figure 4d, considering the occurrence of the Changning M_s 6.0
228 earthquake sequence, the distribution area of low b values expands in the NW direction, and the lowest
229 b value is about 0.501, which is close to that in Figure 4c. Compared with the results obtained by ignoring
230 the depth information of the earthquake in Figure 4a-b, the results obtained by Figure 4c-d reveal more
231 significant heterogeneity of b values. When investigating this problem to the depth of the crust. Lower b
232 values may indicate that there should be greater differential stress at the depth where the source area of
233 the mainshock is located, and it is easily ignored by b value calculations that usually do not consider the
234 depth information of earthquake events.

235

236

Fig. 4

237 Figure 5 shows the spatial distribution of the median absolute deviation (MAD) of b values by the data-
238 driven approach according to Figure 4. The ensemble MAD b value is smaller in the most region of
239 Figure 5a-d, especially in the rectangular region A'B'C'D', which implies that these regions have
240 relatively stable distribution and reliable ensemble median b values. As a comparison with Figures 4 and
241 Figure 5, we also used the Changning M_S 6.0 earthquake and aftershocks to calculate the ensemble MAD
242 b values and the ensemble MAD b values. For the corresponding results, please see Figure S2 in the
243 *Supplementary Materials*.

244

245

Fig. 5

246 Spatiotemporal Heterogeneity of b values

247 Considering that b value usually changes over time before and after a strong earthquake, this paper not
248 only examines the spatial distribution of b values in the surface and depth profiles but also discusses the
249 spatiotemporal distribution of b values for earthquake events in the rectangular area A'B'C'D' where the
250 Changning M_S 6.0 sequence is located. Due to the strong temporal and spatial inhomogeneity of seismic
251 activity, especially clustering in time, this brings great difficulties to obtaining a stable and reliable b
252 value and clearly showing the temporal and spatial variation of the b value. In order to reduce this
253 difficulty to a certain extent, here we use the index of earthquake occurrence instead of time, that is, the
254 earthquake is projected on a pseudo-time axis of the index number of the occurrence time sequence.
255 Using the same calculation method as in Figure 4 and Figure 5, the distributions of ensemble median b
256 values and ensemble MAD b values on the distance-index map are obtained. The corresponding results
257 are shown in Figure 6 and Figure 7. Considering the possible abrupt change of the regional stress field
258 due to strong earthquakes such as the Changning M_S 6.0 earthquake, we adopt two schemes to study the
259 spatiotemporal distribution of b values. One is to study the seismicity before and after the mainshock as
260 a whole, and the other is to study the seismicity before and after the mainshock as two independent
261 periods. The calculation results under the two schemes are shown in Figure 6a-b, respectively.

262

263

Fig. 6

264 It can be seen in Figure 6a that before the Changning M_s 6.0 earthquake, in the segment between -5 km
265 and -10 km near the A'/B' end and a length of about 10 km (NW direction of the aftershocks in Fig. 1),
266 showed relatively stable high b values, with the maximum value exceeding 2.0. In the segment between
267 -5 km and 12 km near the C'/D' end and a length of about 17 km (the SE direction of the aftershocks in
268 Figure 1, including the nucleation point of the mainshock), showed relatively stable low values before
269 the Changning M_s 6.0 earthquake, and the range of the low b values gradually narrowed down and
270 concentrated towards the nucleation point of the mainshock. After the Changning M_s 6.0 earthquake
271 occurred, the b values in the entire spatial range from A'/B' to C'/D' decreased significantly. Among them,
272 the b values in the 0 km ~ 12 km segment where the nucleation point of the mainshock is located have
273 recovered rapidly, while the b values in the 0 km ~ -15 km segment have increased at a slower rate.
274 From the results before and after the Changning M_s 6.0 earthquake shown in Figure 6b, it can be seen
275 that the occurrence of the mainshock has a greater impact on the continuity of time variant b values. This
276 means that the spatiotemporal evolution image of the b values given in Figure 6a over the entire study
277 period is not physically valid. Correspondingly, the decrease of pre-mainshock b values and the sudden
278 expansion of the low b values may be a kind of artifact caused by the subsequent aftershocks brought
279 into the calculation (Lei et al., 2019).

280 Compared with Figure 6a, the results in Figure 6b show that before the Changning M_s 6.0 earthquake,
281 the shortening and concentration changes for the low b value_segment near the C'/D' end, and the
282 expansion process of the high b value segment on the near the A'/B' end is performed simultaneously.
283 This implies that a significantly higher differential stress area is concentrated toward the nucleation point
284 of the mainshock. Figure 7 a-b show the distribution of ensemble MAD b values according to Figure 6
285 a-b, where higher ensemble MAD b values mainly appear in some areas with higher b values in Figure
286 6 a-b.

287

288

Fig. 7

289 **Discussion**

290 In the pattern of b value spatial heterogeneity before strong earthquakes, the locations of rupture
291 nucleation points, sliding distributions, and aftershock distributions of some strong earthquakes were
292 observed to correspond to areas with lower b values, such as the Parkfield $M = 6.0$ earthquake on
293 September 28, 2004 (Wiemer and Wyss, 1997; Schorlemmer et al., 2004; Schorlemmer and Wiemer,
294 2005). However, the significant spatial heterogeneity of b values obtained from the studies of these
295 earthquakes is suspected to be related to the subjective arbitrariness of the calculation rules (Kamer and
296 Hiemer, 2015). The calculation results based on the data-driven method (Si and Jiang, 2019) in this paper
297 show that significant spatial heterogeneity of b values can still be observed before the Changning $M_{\text{S}} 6.0$
298 earthquake, especially on the depth profile of the fault. Moreover, according to the empirical relationship
299 between the magnitude and rupture scale of Wells and Coppersmith (1994), the low-value spatial scale
300 of $b < 0.75$ in Figure 4c is also close to the rupture length of about 10 km for the $M 6.0$ mainshock. This
301 also means that it is still feasible to use the spatial heterogeneity of the b values to identify the locked
302 asperities and determine the location of future strong earthquakes if more cases are verified.
303 There is still much controversy over the temporal variation pattern of b values in the source area before
304 a strong earthquake. Although the decrease of b values prior to failure was found in laboratory fracturing
305 experiments on relatively complete rock samples (e.g., Thompson et al., 2006; Lei, 2019) and the case
306 study of strong earthquakes (Nanjo et al., 2012; Schurr et al., 2014; Bayrak et al., 2017; Huang et al.,
307 2020), but a large number of reported temporal variations of b values before actual strong earthquakes
308 are still considered to have no statistically significant predictive power (Parsons, 2007). Some studies
309 have found that the temporal variation of b values corresponding to asperities are synchronized with
310 loading rate and shear stress (Tormann et al., 2013). Schorlemmer et al. (2004) and Wiemer and Wyss
311 (2002) studied some earthquake cases and concluded that the b value is quite stable over time and it is
312 difficult to observe a significant change. The study of the relationship between acoustic emission events
313 and stress in the stick-slip experiment shows that the complexity of the temporal variations of b values
314 observed when sliding on rough fault planes may be due to fault-structure heterogeneity (Goebel et al.,
315 2013). In this study of the Changning $M_{\text{S}} 6.0$ earthquake, we did not simply examine the temporal
316 variations of b values in a fixed spatial range, but investigated the migration pattern of the b value in a
317 2-D spatiotemporal dimension. We found that as the time approaches the occurrence of the mainshock,

318 the spatial range of the low b values gradually shrinks and focuses on the vicinity of the rupture nucleation
319 point, and the b values does not decrease significantly. Under the assumption that the fault-structural
320 heterogeneity will not change in the short term, and based on previous understandings of the correlation
321 between high b values and fluid-induced seismicity, the migration pattern in this paper may be explained
322 by the erosion of fluid in the high differential stress area where the nucleation point is located.

323 For the spatiotemporal heterogeneity of the b value of the aftershocks of the 2019 Changning M_s 6.0
324 earthquake, we noticed that the aftershocks expanded spatially to areas with high pre-mainshock b values
325 in the northwest direction, and the length of the aftershock area was significantly longer than the rupture
326 scale of the earthquake (see Fig. 6b). Since the aftershocks do not exhibit relatively slow spatiotemporal
327 migration behavior, the physical mechanism that drives the aftershocks of this earthquake cannot be
328 explained by either the traditional stress corrosion model (Das and Scholz, 1981), or by frictional afterslip
329 model (Perfettini et al., 2018; Koper et al., 2018). Some views suggest that aftershock activity in high b
330 value regions may be related to the reactivation of highly fractured fault zones, the redistribution of stress
331 fields, and the role of fluids trapped in microfractures (Aktar et al., 2004). Long et al. (2020) imaging the
332 velocity structure of the area where the Changning M_s 6.0 earthquake was located, showing that there is
333 an obvious S-wave low-velocity anomaly at the depth of 3 to 8 km in the northwestern segment of the
334 aftershock. In this paper, this S-wave low-velocity anomaly region also corresponds to the distribution
335 of high b values, which may be related to the fluid intrusion. Therefore, we deduce that the abundant
336 aftershocks produced by this mainshock, and the active area that exceeds the rupture scale of the
337 mainshock are more likely to be caused by the mainshock which triggered a series of complex structural
338 aftershocks northwest of the nucleation point. The dynamic expansion of the high pre-mainshock b value
339 region to the nucleation point also creates conditions for the triggering of a large number of aftershocks
340 and the widespread spatially.

341 In addition, b values of the aftershocks first dropped rapidly to about 0.5, then gradually recovered, and
342 returned to the pre-seismic level after the fourth magnitude 5 strong aftershock (excluding high b value
343 areas). The phenomenon that the b values of the aftershock sequence decreases immediately after the
344 mainshock to a rapid recovery has been observed in many earthquake cases (El-Isaa and Eatonb, 2014;
345 Tormann et al., 2015). Unlike most aftershock sequences, where the b value generally increases by 20%
346 after the mainshock, this sudden decrease in b value is considered to be related to the occurrence of
347 subsequent strong aftershocks or larger earthquakes (Gulia and Wiemer, 2019). In the aftershock

348 sequence of the Changning M_s 6.0 earthquake, the rapidly decreasing b value of the aftershocks was
349 accompanied by 4 strong aftershocks with magnitudes greater than 5.0, which is consistent with the
350 phenomenon revealed by previous studies. This may also support the idea of discrimination between
351 foreshocks and aftershocks by real-time monitoring of the b value in aftershock sequences (Gulia and
352 Wiemer, 2019). However, it needs to be pointed out that similar to the problem of sudden changes in the
353 spatiotemporal distribution of b values before and after the main shock, it cannot rule out that 4 strong
354 aftershocks with $M > 5$ will affect the continuity of the b values to a certain extent.

355 **Conclusions**

356 To reveal whether there is spatiotemporal heterogeneity of b values before and after the 2019 Changning
357 M_s 6.0 earthquake, and to overcome the subjectivity of the choice of data used for calculation, we applied
358 the OK1993 model of magnitude-frequency distribution according to the data-driven idea to calculate b
359 values. We also investigated the distribution characteristics of b values from three different ways:
360 horizontal surface distribution, depth profile distribution, and in the distance-rank of index map. The
361 main conclusions are as follows:

362 1. The b values before and after the Changning M_s 6.0 earthquake showed strong spatiotemporal
363 heterogeneity on the horizontal surface distribution, depth profile distribution, and distance-rank of index
364 map. Among them, before the Changning M_s 6.0 earthquake, there were obvious low b value distributions
365 near the epicenter of the mainshock and within the depth range of 3 to 12 km. The correlation shows that
366 there may be significantly higher differential stress in the source area before the Changning M_s 6.0
367 earthquake. The northwestern segment of the aftershocks has a distinctly high b value distribution, which
368 coincides with the S-wave low-velocity anomaly region shown by the velocity structure imaging.

369 2. The b value spatiotemporal distribution results show that before the Changning M_s 6.0 earthquake, the
370 high b value region of the NW segment spread by aftershocks gradually expanded and approached the
371 nucleation point as the time approached the failure time of mainshock. This may be related to the fluid
372 intrusion in the rock. A large number of aftershocks were produced and the area where the aftershocks
373 were spread was significantly larger than the rupture scale of the mainshock. The mainshock may
374 triggered seismicity in the NW direction where the fluid intrudes.

375 3. The b values of the aftershocks of the Changning M_s 6.0 earthquake decreased rapidly and gradually

376 recovered after the mainshock, indicating a higher differential stress level in the aftershock area. The
377 time variation of low b value is synchronized with the occurrence of strong aftershocks with $M \geq 5.0$,
378 showing the application potential that can be used to distinguish between foreshocks and aftershocks.
379 4. Although the distribution characteristics of b values before and after the Changning $M_S 6.0$ earthquake
380 were qualitatively consistent when they were studied in different space-time dimensions, there were
381 significant differences in specific b value. For example, the minimum b value of the Changning $M_S 6.0$
382 earthquake on the depth profile distribution is about 0.493, but it is about 0.732 when the seismic depth
383 information is ignored and only calculated on the surface. This inconsistency needs special attention
384 when studying the spatiotemporal heterogeneity of b values.

385 **Acknowledgment**

386 This study is supported by the program of China Seismic Experimental Site (CSES, No. 2019CSES0106),
387 the program of basic resources investigation of science and technology (No. 2018FY100504), the
388 National Natural Science Foundation of China (No. U2039204), and the Special Fund of the Institute of
389 Geophysics, China Earthquake Administration (No.DQJB20X11). The earthquake catalog used in this
390 paper was provided by the Sichuan Earthquake Agency. The Multi-Parametric Toolbox 3.0
391 (<https://www.mpt3.org/Main/HomePage>, last accessed June 2018) is used for the analysis of parametric
392 optimization and computational geometry. We thank the editor and two anonymous reviewers for their
393 very helpful comments and suggestions.

394 **References**

395 Aktar, M., S. Özalaybey, M. Ergin, H. Karabulut, M.-P. Bouin, C. Tapirdamaz, F. Biçmen, A. Yörük
396 and M. Bouchon (2004). "Spatial variation of aftershock activity across the rupture zone of the 17
397 August 1999 Izmit earthquake, Turkey." *Tectonophysics* **391**(1-4): 325-334.

398 Amelung, F. and G. King (1997). "Earthquake scaling laws for creeping and non-creeping faults."
399 *Geophysical Research Letters* **24**(5): 507-510.

400 Amorèse, D., J.-R. Grasso and P. Rydelek (2010). "On varying b -values with depth: results from
401 computer-intensive tests for Southern California." *Geophysical Journal International* **180**(1): 347-
402 360.

403 Bayrak, E., S. Yilmaz and Y. Bayrak (2017). "Temporal and spatial variations of Gutenberg-Richter
404 parameter and fractal dimension in Western Anatolia, Turkey." Journal of Asian Earth Sciences,
405 **138**: 1-11.

406 Das, S. and C. Scholz (1981). "Theory of time-dependent rupture in the Earth." Journal of
407 Geophysical Research: Solid Earth **86**(B7): 6039-6051.

408 Del Pezzo, E., F. Bianco and G. Saccorotti (2003). "Duration magnitude uncertainty due to seismic
409 noise: Inferences on the temporal pattern of GR *b*-value at Mt. Vesuvius, Italy." Bulletin of the
410 Seismological Society of America **93**(4): 1847-1853.

411 El-Isaa, Z. H. and D. W. Eatonb (2014). "Spatiotemporal variations in the *b*-value of earthquake
412 magnitude-frequency distributions: Classification and causes." Tectonophysics **615-616**: 1-11.

413 Goebel, T. H. W., D. Schorlemmer, T. Becker, G. Dresen and C. Sammis (2013). "Acoustic
414 emissions document stress changes over many seismic cycles in stick-slip experiments."
415 Geophysical Research Letters **40**(10): 2049-2054.

416 Gulia, L. and S. Wiemer (2019). "Real-time discrimination of earthquake foreshocks and
417 aftershocks." Nature **574**(7777): 193-199.

418 Gulia, L., S. Wiemer and D. Schorlemmer (2010). "Asperity-based earthquake likelihood models
419 for Italy." Annals of Geophysics **53**(3): 63-75.

420 Hainzl, S. and T. Fischer (2002). "Indications for a successively triggered rupture growth underlying
421 the 2000 earthquake swarm in Vogtland/NW Bohemia." Journal of Geophysical Research: Solid
422 Earth **107**(B12): ESE 5-1-ESE 5-9.

423 Huang, H., L. S. Meng, R. Bürgmann, W. Wang and K. Wang (2020). "Spatio-temporal foreshock
424 evolution of the 2019 M 6.4 and M 7.1 Ridgecrest, California earthquakes." Earth and Planetary
425 Science Letters, **551**: 116582.

426 Hutton, K., J. Woessner and E. Hauksson (2010). "Earthquake monitoring in southern California
427 for seventy-seven years (1932–2008)." Bulletin of the Seismological Society of America **100**(2):
428 423-446.

429 Kagan, Y. Y. (1999). "Universality of the seismic moment-frequency relation." Pure and Applied
430 Geophysics **155**(2): 537-573.

431 Kamer, Y. and S. Hiemer (2015). "Data-driven spatial b value estimation with applications to
432 California seismicity: To b or not to b ." Journal of Geophysical Research: Solid Earth **120**(7): 5191-
433 5214.

434 Koper, K. D., K. L. Pankow, J. C. Pechmann, J. M. Hale, R. Burlacu, W. L. Yeck, H. M. Benz, R.
435 B. Herrmann, D. T. Trugman and P. M. Shearer (2018). "Afterslip enhanced aftershock activity
436 during the 2017 earthquake sequence near Sulphur Peak, Idaho." Geophysical Research Letters
437 **45**(11): 5352-5361.

438 Lei, X. L. (2019). "Evolution of b -value and fractal dimension of acoustic emission events during
439 shear rupture of an immature fault in Granite." Applied Sciences **9**(12): 2498.

440 Lei, X. L. and T. Satoh (2007). "Indicators of critical point behavior prior to rock failure inferred
441 from pre-failure damage." Tectonophysics **431**(1-4): 97-111.

442 Lei, X., Z. Wang and J. Su (2019). "Possible link between long-term and short-term water injections
443 and earthquakes in salt mine and shale gas site in Changning, south Sichuan Basin, China." Earth
444 and Planetary Physics **3**(6): 510-525.

445 Long, F., Z. Zhang, Y. Qi, M. Liang, X. Ruan, W. Wu, G. Jiang and L. Zhou (2020). "Three
446 dimensional velocity structure and accurate earthquake location in Changning-Gongxian area of
447 southeast Sichuan." Earth and Planetary Physics **4**(2): 1-15.

448 Mori, J. and R. E. Abercrombie (1997). "Depth dependence of earthquake frequency-magnitude
449 distributions in California: Implications for rupture initiation." Journal of Geophysical Research:
450 Solid Earth **102**(B7): 15081-15090.

451 Murru, M., R. Console, G. Falcone, C. Montuori and T. Sgroi (2007). "Spatial mapping of the b
452 value at Mount Etna, Italy, using earthquake data recorded from 1999 to 2005." Journal of
453 Geophysical Research: Solid Earth **112**: B12303.

454 Nandan, S., G. Ouillon, S. Wiemer and D. Sornette (2017). "Objective estimation of spatially
455 variable parameters of epidemic type aftershock sequence model: Application to California."
456 Journal of Geophysical Research: Solid Earth **122**(7): 5118-5143.

457 Nanjo, K. Z., N. Hirata, K. Obara and K. Kasahara (2012). "Decade - scale decrease in b value prior
458 to the M9 - class 2011 Tohoku and 2004 Sumatra quakes." *Geophysical Research Letters* **39**:
459 L20304.

460 Ogata, Y. (2011). "Significant improvements of the space-time ETAS model for forecasting of
461 accurate baseline seismicity." *Earth, Planets and Space* **63**(3): 6.

462 Ogata, Y. and K. Katsura (1993). "Analysis of temporal and spatial heterogeneity of magnitude
463 frequency distribution inferred from earthquake catalogues." *Geophysical Journal International*
464 **113**(3): 727-738.

465 Parsons, T. (2007). "Forecast experiment: Do temporal and spatial b value variations along the
466 Calaveras fault portend $M \geq 4.0$ earthquakes?" *Journal of Geophysical Research: Solid Earth*
467 **112**(B3): B03308.

468 Perfettini, H., W. Frank, D. Marsan and M. Bouchon (2018). "A model of aftershock migration
469 driven by afterslip." *Geophysical Research Letters* **45**(5): 2283-2293.

470 Rubner, Y., C. Tomasi, L. J. Guibas (2000). "The earth mover's distance as a metric for image
471 retrieval." *International Journal of Computer Vision* **40**: 99-121.

472 Sambridge, M., T. Bodin, K. Gallagher and H. Tkalčić (2013). "Transdimensional inference in the
473 geosciences." *Philosophical Transactions of the Royal Society A: Mathematical, Physical and*
474 *Engineering Sciences* **371**(1984): 20110547.

475 Scholz, C. H. (1968). "The frequency-magnitude relation of microfracturing in rock and its relation
476 to earthquakes." *Bulletin of the seismological society of America* **58**(1): 399-415.

477 Schorlemmer, D. and S. Wiemer (2005). "Microseismicity data forecast rupture area." *Nature*
478 **434**(7037): 1086-1086.

479 Schorlemmer, D., S. Wiemer and M. Wyss (2004). "Earthquake statistics at Parkfield: 1. Stationarity
480 of b values." *Journal of Geophysical Research: Solid Earth* **109**(B12).

481 Schurr B, G. Asch, S. Hainzl, J. Bedford, A. Hoechner, M. Palo, R. Wang, M. Moreno, M. Bartsch,
482 Y. Zhang, O. Oncken, F. Tilmann, T. Dahm, P. Victor, S. Barrientos and J. Vilote (2014). "Gradual

483 unlocking of plate boundary controlled initiation of the 2014 Iquique earthquake." *Nature* **512**: 299-
484 302.

485 Si, Z. Y. and C. S. Jiang (2019). "Research on parameter calculation for the Ogata–Katsura 1993
486 model in terms of the frequency–magnitude distribution based on a data-driven approach."
487 *Seismological Research Letters* **90**(3): 1318-1329.

488 Stirling, M. W., S. G. Wesnousky and K. Shimazaki (1996). "Fault trace complexity, cumulative
489 slip, and the shape of the magnitude-frequency distribution for strike-slip faults: A global survey."
490 *Geophysical Journal International* **124**(3): 833-868.

491 Svec, L., S. Burden, A. Dilley (2007). "Applying Voronoi diagrams to the redistricting problem."
492 *The UMAP Journal* **28**: 313-32.

493 Thompson, B. D., R. P. Young and D. A. Lockner (2006). "Fracture in Westerly granite under AE
494 feedback and constant strain rate loading: nucleation, quasi-static propagation, and the transition to
495 unstable fracture propagation." *Pure and Applied Geophysics* **163**(5-6): 995-1019.

496 Toda, S., R. S. Stein, P. A. Reasenberg, J. H. Dieterich and A. Yoshida (1998). "Stress transferred
497 by the 1995 $M_w=6.9$ Kobe, Japan, shock: Effect on aftershocks and future earthquake probabilities."
498 *Journal of Geophysical Research: Solid Earth* **103**(B10): 24543-24565.

499 Tormann, T., B. Enescu, J. Woessner, and S. Wiemer (2015). "Randomness of megathrust
500 earthquakes implied by rapid stress recovery after the Japan earthquake." *Nature Geoscience* **8**: 152-
501 158.

502 Tormann, T., S. Wiemer, S. Metzger, A. Michael, and J. L. Hardebeck (2013). "Size distribution of
503 Parkfield's microearthquakes reflects changes in surface creep rate." *Geophysical Journal
504 International* **193**: 1474-1478.

505 Urbancic, T. I., C. I. Trifu, J. M. Long and R. P. Young (1992). "Space-time correlations of b values
506 with stress release." *Pure and Applied Geophysics* **139**(3-4): 449-462.

507 Waldhauser, F. and W. L. Ellsworth (2000). "A double-difference earthquake location algorithm:
508 method and application to the Northern Hayward fault, California." *Bulletin of the Seismological
509 Society of America* **90**(6): 1353-1368.

510 Wells, D. L. and K. J. Coppersmith (1994). "New empirical relationships among magnitude, rupture
511 length, rupture width, rupture area, and surface displacement." Bulletin of the seismological Society
512 of America **84**(4): 974-1002.

513 Wiemer, S. and D. Schorlemmer (2007). "ALM: An asperity-based likelihood model for
514 California." Seismological Research Letters **78**(1): 134-140.

515 Wiemer, S. and M. Wyss (1997). "Mapping the frequency-magnitude distribution in asperities: An
516 improved technique to calculate recurrence times?" Journal of Geophysical Research: Solid Earth
517 **102**(B7): 15115-15128.

518 Wiemer, S. and M. Wyss (2002). Mapping spatial variability of the frequency-magnitude
519 distribution of earthquakes. Advances in Geophysics **45**: 259-302.

520 Woessner, J. and S. Wiemer (2005). "Assessing the quality of earthquake catalogues: Estimating
521 the magnitude of completeness and its uncertainty." Bulletin of the Seismological Society of
522 America **95**(2): 684-698.

523 Wyss, M. (1973). "Towards a physical understanding of the earthquake frequency distribution."
524 Geophysical Journal of the Royal Astronomical Society **31**(4): 341-359.

525 Wyss, M., D. Schorlemmer and S. Wiemer (2000). "Mapping asperities by minima of local
526 recurrence time: San Jacinto-Elsinore fault zones." Journal of Geophysical Research: Solid Earth
527 **105**(B4): 7829-7844.

528 Xie, J., S. Ni and X. Zeng (2012). "1 D shear wave velocity structure of the shallow upper crust in
529 central Sichuan Basin." Earthquake Research in Sichuan (in Chinese) **143**(2): 20-24.

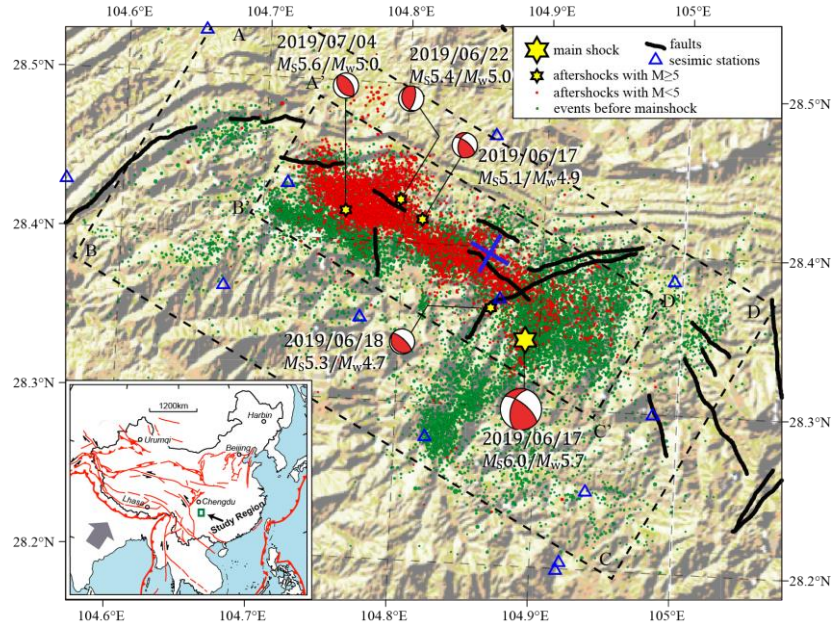
530 Yi, G. X., F. Long, M. J. Liang, M. Zhao, S. W. Wang, Y. Gong, H. Z. Qiao and J. R. Su (2019).
531 "Focal mechanism solutions and seismogenic structure of the 17 June 2019 M_s 6.0 Sichuan
532 Changning earthquake sequence." Chinese Journal of Geophysics (in Chinese) **62**(9): 3432-3447.

533

534

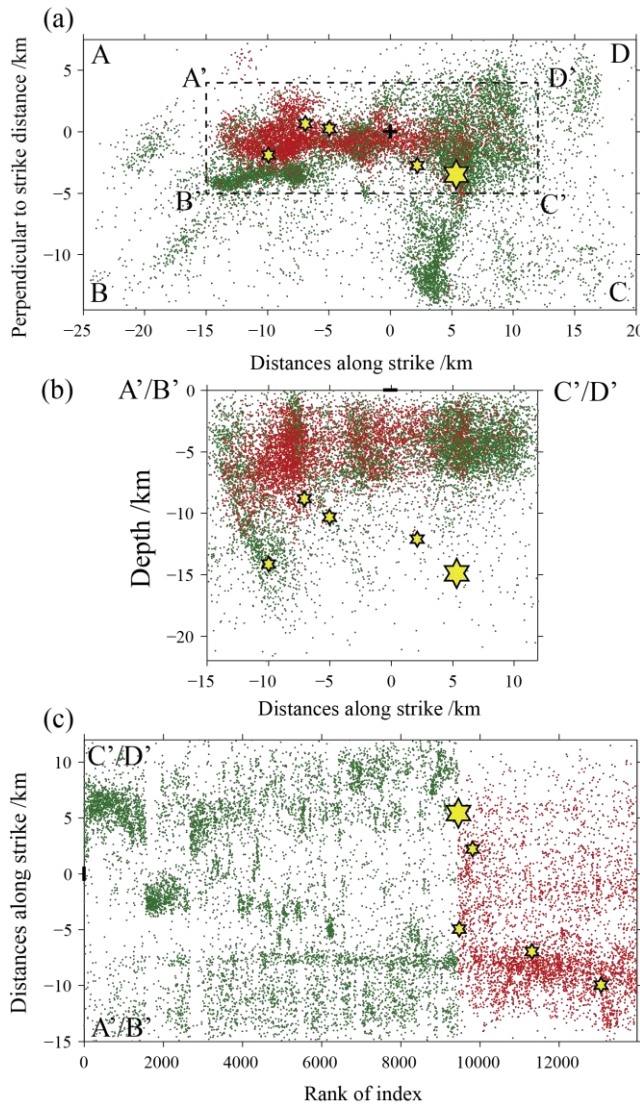
535

536



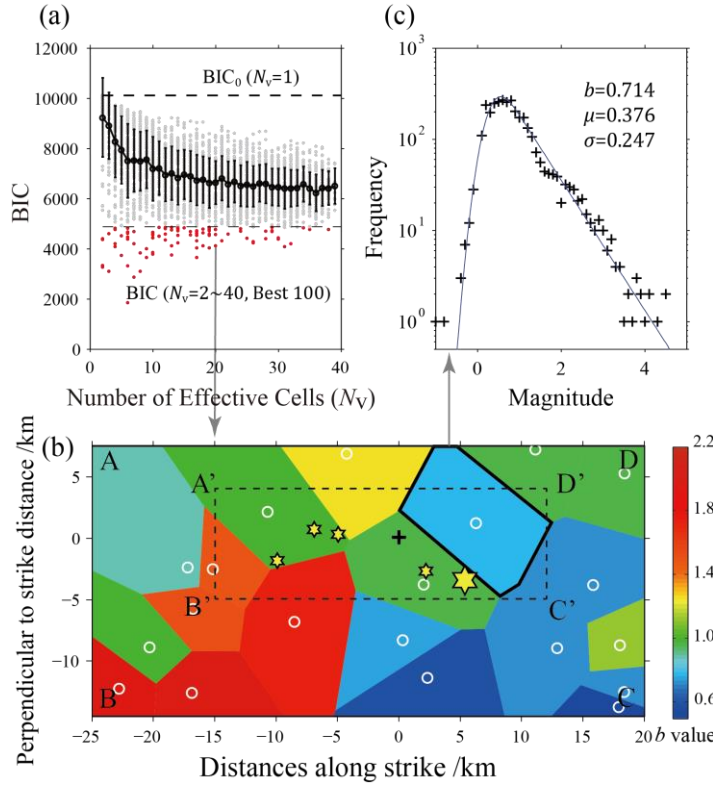
537

538 **Fig. 1 Distribution of seismicity in the Changning area. The red dots show the aftershocks of the Changning**
 539 **$M_s 6.0$ earthquake, and the green dots indicate the earthquakes that occurred before the Changning**
 540 **$M_s 6.0$ earthquake. Hexagonal stars mark the position of the mainshock and four aftershocks with**
 541 **magnitude no less than 5.0, and the corresponding focal mechanisms are marked. The dotted**
 542 **rectangular ABCD and A'B'C'D' show the two spatial regions for calculating the b value and rotating**
 543 **the coordinate system, and the blue cross symbol gives the origin where the coordinate system is**
 544 **rotated. The blue triangles show the location of seismic stations that record these earthquakes, and the**
 545 **solid black lines represent active faults (He et al., 2019). The study region is shown in the location**
 546 **figure in the bottom-left by a green rectangle.**



547

548 **Fig. 2 Distribution of seismicity for b values calculations.** (a) Rotating the coordinate system to the seismic
 549 distribution along the direction of the aftershock distribution; (b) Projecting the earthquakes in the
 550 rectangular frame $A'B'C'D'$ on the depth profile; (c) The temporal and spatial distribution on the
 551 distance versus rank of index 2-D map of the earthquakes within the rectangular frame $A'B'C'D'$. The
 552 meaning of the symbols is the same as in Fig. 1.

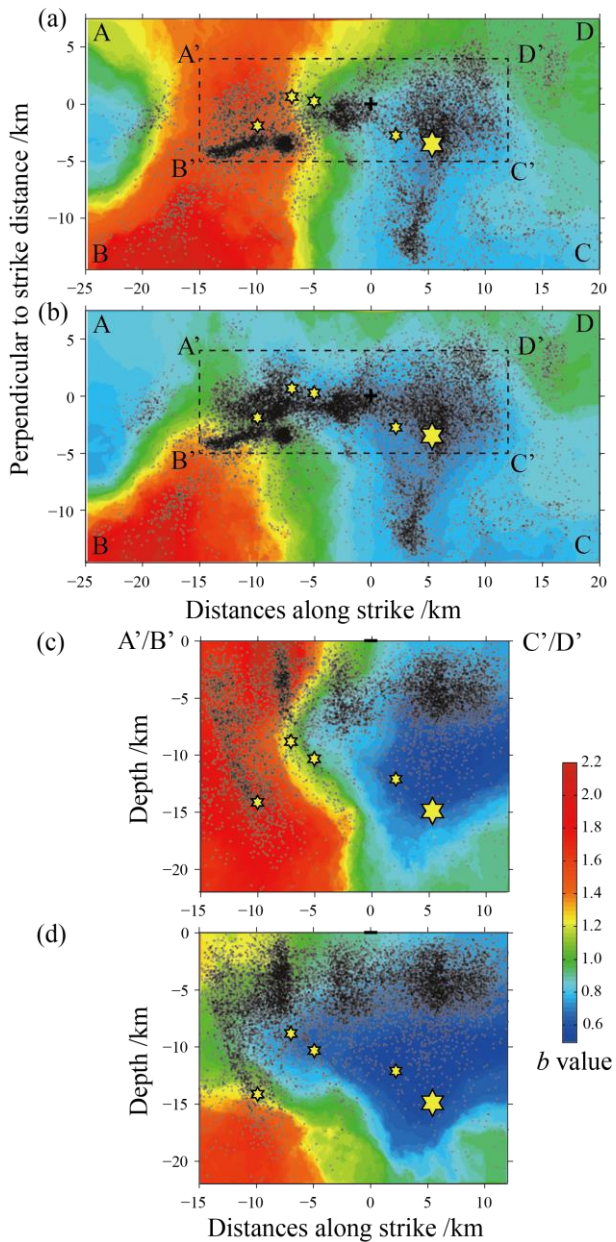


553

554 **Fig. 3** An example of calculating the parameters of the Ogata-Katsura 1993 model in terms of the frequency-
 555 magnitude distribution based on a data-driven approach. (a) Distribution of BIC values versus the
 556 number of effective cells N_v in the Voronoi tessellation. The black dots and error bars are
 557 commensurate with the mean value and one standard deviation of BIC values under the corresponding
 558 N_v , respectively. The top horizontal dashed line marks the BIC values of the entire spatial region
 559 without mesh generation ($BIC_0, N_v = 1$). The red dots show the BIC values with the best-100 solutions
 560 are selected, while the gray dots are the other BIC results according to N_v . (b) Example of Voronoi
 561 tessellation of $N_v=20$ and one of the best-100 models selected. The white circles are the positions of the
 562 Voronoi nodes, and the resulting partitions are color coded by their estimated b values (obtained from
 563 the β -value in the Ogata-Katsura 1993 model). (c) Example of fitting result for the frequency-
 564 magnitude distribution (FMD) of the Ogata-Katsura 1993 (OK1993) model in the Voronoi cell
 565 indicated by a thick line in subgraph (b).

566

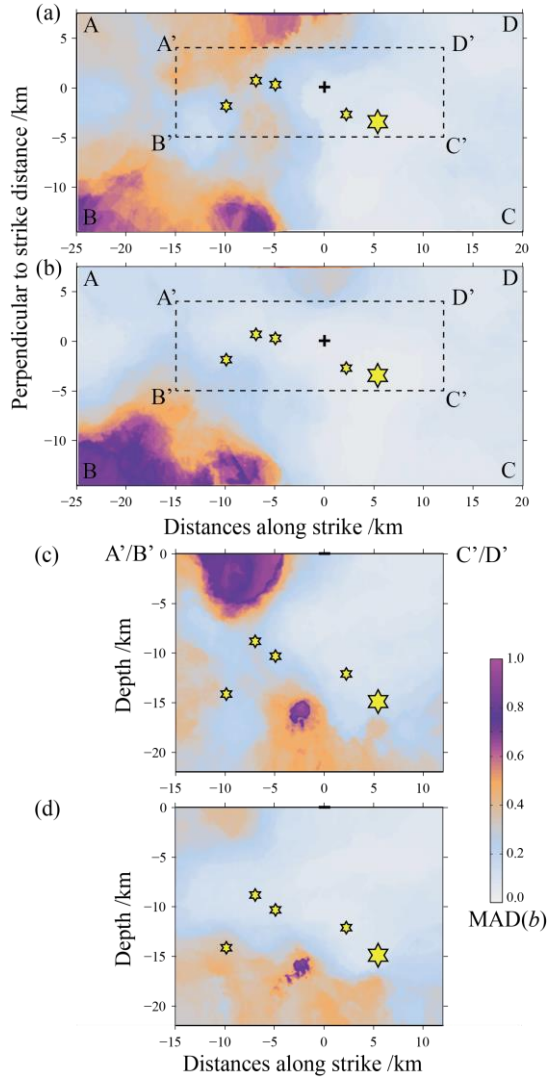
567



568

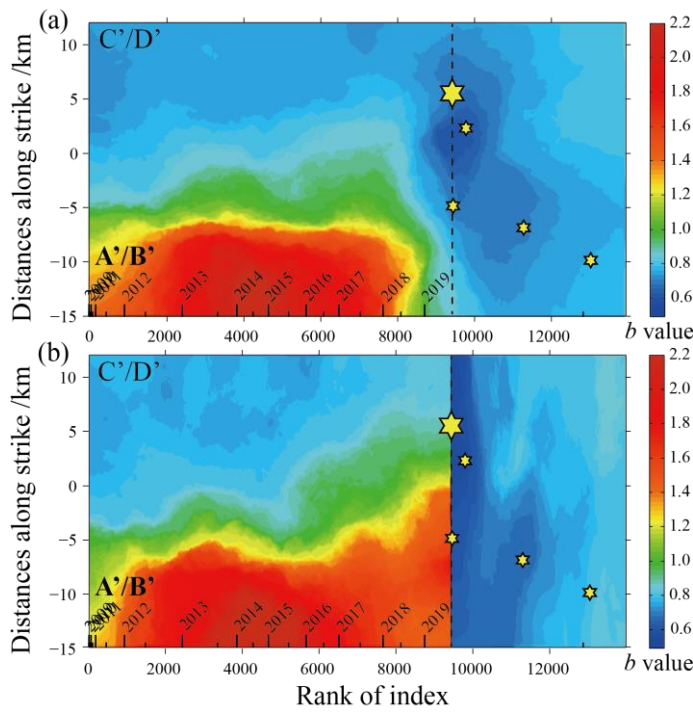
569 **Fig. 4** The spatial distribution of the ensemble median b values of the best-100 solutions for $N_v=2\sim 40$ in the
 570 Changning area. (a) The ensemble median b values before the Changning $M_s 6.0$ earthquake is
 571 distributed on the horizontal plane after the rotation; (b) The ensemble median b values obtained by
 572 calculation of all the earthquake including the aftershocks of the Changning $M_s 6.0$ earthquake is
 573 distributed on the horizontal plane after the rotation; (c) distribution of the ensemble median b values

574 before the occurrence of the Changning M_s 6.0 earthquake in the rectangular frame A'B'C'D' on the
575 depth profile; (d) distribution of ensemble median b values obtained by calculation of all earthquakes
576 including aftershocks of the Changning M_s 6.0 earthquake in the rectangular frame A'B'C'D' on the
577 depth profile. The black dots on each subgraphs mark the seismic events used in the calculation.

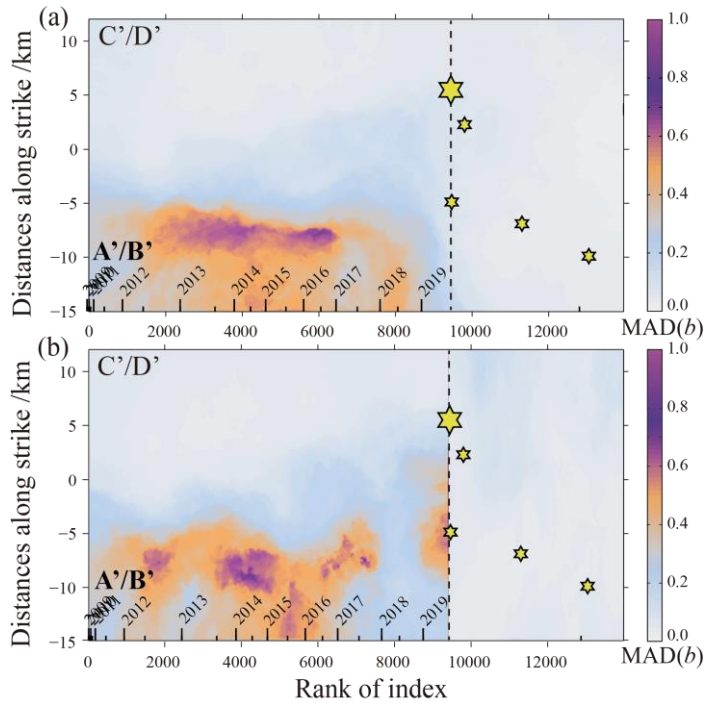


578

579 **Fig. 5** The spatial distribution of the median absolute deviation (MAD) of the b values by the data-driven
 580 approach according to figure 4. (a) The ensemble MAD b values before the Changning M_s 6.0
 581 earthquake is distributed on the horizontal plane after the rotation; (b) The ensemble MAD b values
 582 obtained by calculation of all the earthquake including the aftershocks of the Changning M_s 6.0
 583 earthquake is distributed on the horizontal plane after the rotation; (c) distribution of the ensemble
 584 MAD b values before the occurrence of the Changning M_s 6.0 earthquake in the rectangular frame
 585 A'B'C'D' on the depth profile; (d) distribution of ensemble MAD b values obtained by calculation of
 586 all earthquakes including aftershocks of the Changning M_s 6.0 earthquake in the rectangular frame
 587 A'B'C'D' on the depth profile.



590 **Fig. 6** Spatiotemporal distribution of the ensemble median b values of the best-100 solutions for $N_v=2\sim40$ on
 591 a 2-D space consisting of distance along strike and rank of index. (a) The ensemble median b values
 592 obtained from all data before and after the Changning $M_s 6.0$ earthquake; (b) The ensemble median b
 593 values obtained from the data before and after the Changning $M_s 6.0$ earthquake, respectively. The
 594 vertical dotted line shows where the $M_s 6.0$ earthquake occurred. The time scale is marked at the upper
 595 x -axis, including the time of whole year marked by long tick and the half-year time marked by short
 596 tick.



599 **Fig. 7 Spatiotemporal distribution of the median absolute deviation (MAD) of the b values of the best-100**
600 **solutions for $N_v=2\sim40$ on a 2-D space consisting of distance along strike and rank of index. (a) The**
601 **ensemble MAD b values obtained from all data before and after the Changning $M_s 6.0$ earthquake; (b)**
602 **The ensemble MAD b values obtained from the data before and after the Changning $M_s 6.0$ earthquake,**
603 **respectively. The vertical dotted line shows where the $M_s 6.0$ earthquake occurred. The time scale is**
604 **marked at the upper x -axis, including the time of whole year marked by long tick and the half-year**
605 **time marked by short tick.**